Contract No:

This document was prepared in conjunction with work accomplished under Contract No. 89303321CEM000080 with the U.S. Department of Energy (DOE) Office of Environmental Management (EM).

Disclaimer:

Impact of Glass Iradiation on Laser-induced Breakdown Spectroscopy Diagnostics in the Visible and NIR Range

L. J. Garrett[a], B. W. Morgan[a], M. Burger[a], Y. Lee[b], H. Kim[d], P. Sabharwall[c], S. Choi[d], I. Jovanovic[a]

[a]*Department of Nuclear Engineering and Radiological Sciences, University of Michigan, Ann Arbor, MI 48109, United States*
[b]*Department of Nuclear and Quantum Engineering, Korea Advanced Institute of Science and Technology, 291 Daehak-ro, Yuseong-gu, Daejeon 34141, Republic of Korea*
[c]*Idaho National Laboratory, Idaho Falls, ID 83415, United States*
[d]*Department of Nuclear Engineering, Seoul National University, 1 Gwanak-ro, Gwanak-gu, Seoul 08826, Republic of Korea*

Abstract

Increased absorption of optical materials arising from the exposure to ionizing radiation must be accounted for to accurately analyze the laser-induced breakdown spectroscopy (LIBS) data retrieved from high-radiation environments. We evaluate this effect on a specific example that mimics the diagnostics placed within a gas-cooled fast reactor coolant stream. Analysis is performed on the LIBS data measured with 1% Xe gas in an ambient He environment and the measured optical absorption from the gamma- and neutron-irradiated low-OH fused silica and sapphire glasses. No significant change in the number of shots required to reach a 3σ detection level was observed up to 10 Mrad gamma dose and exposure to a 1.7×10^{17} n/cm^2 neutron fluence. In contrast, the spectral dependence of absorption results in either a systematic overestimation or underestimation of line intensity ratios, depending on the line of interest selected for analysis. Moreover, if lines from different spectral regions are used to create Boltzmann plots, this attenuation also leads to statistically significant changes in the calculated temperatures for calculations using Xe II lines only, lowering them from 8000±610 K to 6800±810 K for the case of exposure to the 1.7×10^{17} n/cm^2 flux, and broadening the temperature range required for a 95% confidence interval. In the case of measuring the Xe spectrum, these effects may be mitigated using only the longer-wavelength spectral region, where radiation-attenuation is relatively small, or through analysis using the iterative Saha-Boltzmann method.

Keywords: laser-induced spectroscopy (LIBS), gamma irradiation, neutron irradiation, advanced reactor, linear absorption

1. Introduction

There is significant interest in the development of optical spectroscopy instrumentation for diagnostic applications in advanced reactor systems [1–5]. LIBS has been proposed as a candidate for instrumentation due to multiple capabilities, such as not requiring sample preparation, its sensitivity to non-radioactive materials, its compatibility with analytes of arbitrary phase or composition, and its ability to make remote measurements [6, 7]. In LIBS, a high-power laser pulse, typically in the nanosecond range, is focused onto a sample, leading to ionization of the material through mechanisms such as multiphoton ionization and inverse bremsstrahlung [6, 8].

However, the deployment of LIBS instrumentation in nuclear reactors will likely require that the optical components such as windows, lenses, and fibers be exposed to high doses of ionizing radiation. For successful LIBS implementation, these optics must remain optically transparent to both the excitation source (driving laser) as well as the plasma emission. It is well-known that optical materials such as glass experience damage at the atomic and molecular level that results in macroscopic changes to the material properties such as linear absorption and refractive index [9–12]. If not accounted for, the altered linear absorption could in turn alter the perceived spectral line intensities when the plasma emission is transmitted through optics. Because

Email addresses: lgarr@umich.edu (L. J. Garrett), ijov@umich.edu (I. Jovanovic)

these changes are nonuniform across the optical spectrum, more significant increases in absorption occur in the blue to UV spectral region.

Here, we present an analysis framework to predict the effects of irradiation on the analysis of the measured LIBS spectra. Calculations are performed based on linear absorption data from recent irradiation studies [12, 13] and LIBS measurements of 1% Xe in an ambient He environment, which mimic the conditions relevant to gas-cooled fast reactor fuel cladding failure monitoring [2]. Due to the relatively small increases in absorption at the relevant Xe emission wavelengths, the detectability of individual spectral lines was found to be largely unaffected by 10-Mrad gamma irradiation for both the fused-silica glass and sapphire. However, the more pronounced change of transmission induced by exposure to a combined neutron and gamma flux results in a one order of magnitude increase in the number of laser shots required for a statistically significant line intensity measurement. The spectrally dependent nature of the transmission changes was also found to lead to significant errors in measuring the Xe/He line intensity ratio and the extracted physical parameters such as plasma temperature, which can be calculated based on relative line intensities. However, if analysis is focused to lines within the NIR region where attenuation is minimal, all-observed changes become negligible. These results will support the development of corrective calibrations for LIBS systems exposed to large doses of ionizing radiation.

2. Method and Calculation Details

The decrease in spectral line intensity is determined from the measured spectral absorption, quantified as the transmission T:

$$T = 10^{-D_A}, \tag{1}$$

where D_A is the absorbance in the units of optical density (OD). Using linear interpolation, the spectrally-dependent transmission is determined and multiplied by the measured spectrum. Transmission spectra for the materials studied as a function of the radiation dose can be seen in Fig. 1. The effects studied in this work are separated into two categories: those impacted by a single spectral line and those impacted simultaneously by multiple spectral lines.

2.1. Single-Line Effects

Single-line detectability is characterized based on the signal-to-noise ratio (SNR), which is defined as

$$SNR \equiv I_0/\sigma_B. \tag{2}$$

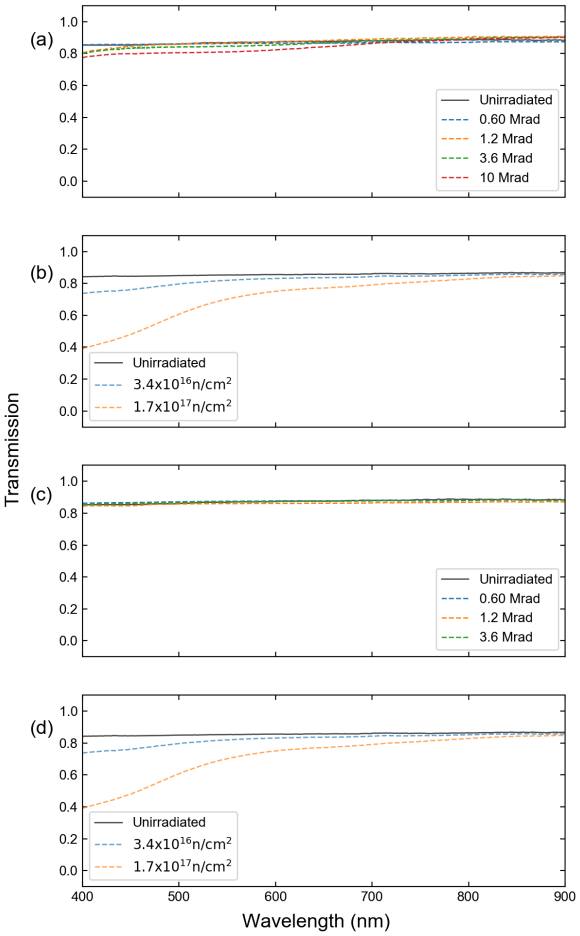

Figure 1: Transmission curves for (a) gamma-irradiated Infrasil-302, (b) neutron-irradiated Infrasil-302, (c) gamma-irradiated sapphire, and (d) neutron-irradiated sapphire windows.

Here, I_0 is the intensity of the spectral line and σ_B is noise, corresponding to the standard deviation of the background. This value was calculated based on the spread observed in the region nearest the spectral line of interest that is devoid of spectral features over a wavelength range equal to the width of the line. The definition of standard deviation dictates that for a stable measurement, the SNR scales as

$$SNR = a\,N^{1/2}, \tag{3}$$

where a represents a fitting constant and N is the number of laser shots. Using this relation, the number of laser shots required to achieve a desired SNR can be estimated. For this study, the detectability limit is defined based on the 3σ criterion, such that lines are considered observable if their peak intensity is at least three times greater than the standard deviation of the background.

Both here and in all further calculations, the peak line intensity is determined by fitting a spectral line to a Voigt profile distribution [14–16], which is given by

$$\frac{I(\lambda)}{I_0} = \frac{2}{\pi}\frac{\lambda_0}{w_l} I_\lambda \int_{-\infty}^{\infty} \frac{exp(-\frac{2.772\lambda_0^2}{w_g^2}(\frac{\nu}{c})^2}{1+\frac{4}{w_l^2}\left[(\lambda-\lambda_0)-\lambda_0(\frac{\nu}{c})\right]^2} d(\frac{\nu}{c}) + y_0. \tag{4}$$

Here, λ_0 is the wavelength at the line center, w_L is the Lorentzian half-width at half maximum (HWHM), w_G is the Gaussian half-width at HWHM, ν is the frequency, c is the speed of light, and y_0 is the vertical offset. The background is defined as a steady region near the peak that covers a span equal to the full-width at the base of the fitted peak as determined by Eq. (4). Once the number of shots required to reach the 3σ detection level is known, the time required is calculated by dividing the number of shots by the laser repetition rate. These calculations are performed with the original experimental data collected with a setup that was not exposed to ionizing radiation, and with the data adjusted for the radiation-induced attenuation.

2.2. Multi-Line Effects

Optical emission line ratios are commonly used to determine the relative component concentrations in a given elemental matrix [17]. Here, the ratio of both the Xe I and the Xe II line intensities were compared to that of the prominent He I line at 587.56 nm. Parameters such as the plasma temperature that can be used for normalization are commonly calculated using the relative line intensities of multiple spectral lines via the Boltzmann plot method [18–20]. In this study, we compare the standard Boltzmann plot method and the Saha-Boltzmann plot method as first described by Yalçin et al. [21] and later adapted by Aguilera and Aragón [22]:

$$\ln\left(\frac{I_0\lambda}{g_j A_{ij}}\right)^* = -\frac{1}{k_B T}E_j^* + \ln\left(\frac{N_0 hc}{Z(T)}\right) \tag{5}$$

In this expression, g_j is the upper level degeneracy, A_{ij} is the transition strength, k_B is the Boltzmann constant, T is the plasma temperature, E_J is the upper level energy, N_0 is the species number density, h is Planck's constant, c is the speed of light, and $Z(T)$ is the partition function. Asterisks denote quantities that must be adjusted for ionic transitions [21, 22]. This method increases the accuracy through the inclusion of spectral lines across the ionization states. The assumption of local thermodynamic equilibrium (LTE) is supported, but not confirmed by the McWhirter criterion. Given as

$$n_e >> 10^{19}\left(\frac{T}{e}\right)^{1/2}\left(\frac{\Delta E}{e}\right)^3 \tag{6}$$

where n_e is the plasma electron density in m^{-3}, e is the fundamental charge and ΔE is the largest difference between subsequent energy levels, this relation describes the threshold at which the electron collision rates surpass radiative decay rates by a sufficient degree for LTE to be achieved [16, 23]. It is assumed that Stark and instrumental broadening are the most significant contributors to spectral line broadening, allowing the plasma density to be calculated as

$$n_e = n_e^{ref}\left(\frac{\Delta\lambda}{w}\right)^{1/m} \tag{7}$$

where n_e^{ref} is a reference electron density value, $\Delta\lambda$ is the Lorentzian component of the spectral line FWHM as determined by 4, w is the line-specific Stark broadening parameter as found in literature, and m is a scaling parameter assumed to approximately equal to 1 [24]. If LTE or near LTE conditions exist, the value calculated using Stark broadening parameters should be in reasonable agreement with the value calculated using the Saha-Eggert equation such that

$$n_e = 2\frac{N_i}{N_j}\frac{Z_j(T)}{Z_i(T)}\left(\frac{m_e k_B T}{2\pi\hbar^2}\right)^{3/2}\exp\left(-\frac{E_\infty - \Delta E}{k_B T}\right).$$

Here, N_i is the atomic population of the i-th quantum state, $Z(T)$ is the partition function of the i-th quantum state, $\hbar$ is the reduced Planck constant, E_∞ is the species ionization energy, and ΔE is a plasma correction factor [16]. Similarly to the single-line effects, the multi-line effects are studied using the experimental LIBS data, which is then adjusted for radiation-induced attenuation.

3. Experiment

3.1. LIBS Data Collection

A schematic of the experimental setup used for the Xe LIBS measurement is shown in Fig. 3. The experimental cell contained a certified mixture of 1% Xe in He (99.999% purity) at room temperature and a pressure of 1.00 bar (1.00×10^5 Pa). Prior to filling, the cell was evacuated to a pressure of 10^{-5} Pa (10^{-7} mbar) to prevent contamination from air. A 1064-nm Nd:YAG laser (Surelite, Continuum) was focused into the cell by a 100-mm focal length lens to induce gas breakdown. The laser produced 10-ns, 250-mJ pulses at a repetition rate of 10 Hz. The resultant LIBS signal was collected using a collimator (CC52, Andor) and directed into an echelle spectrograph (Mechelle, Andor) through a 0.4-mm diameter optical fiber bundle. An intensified CCD

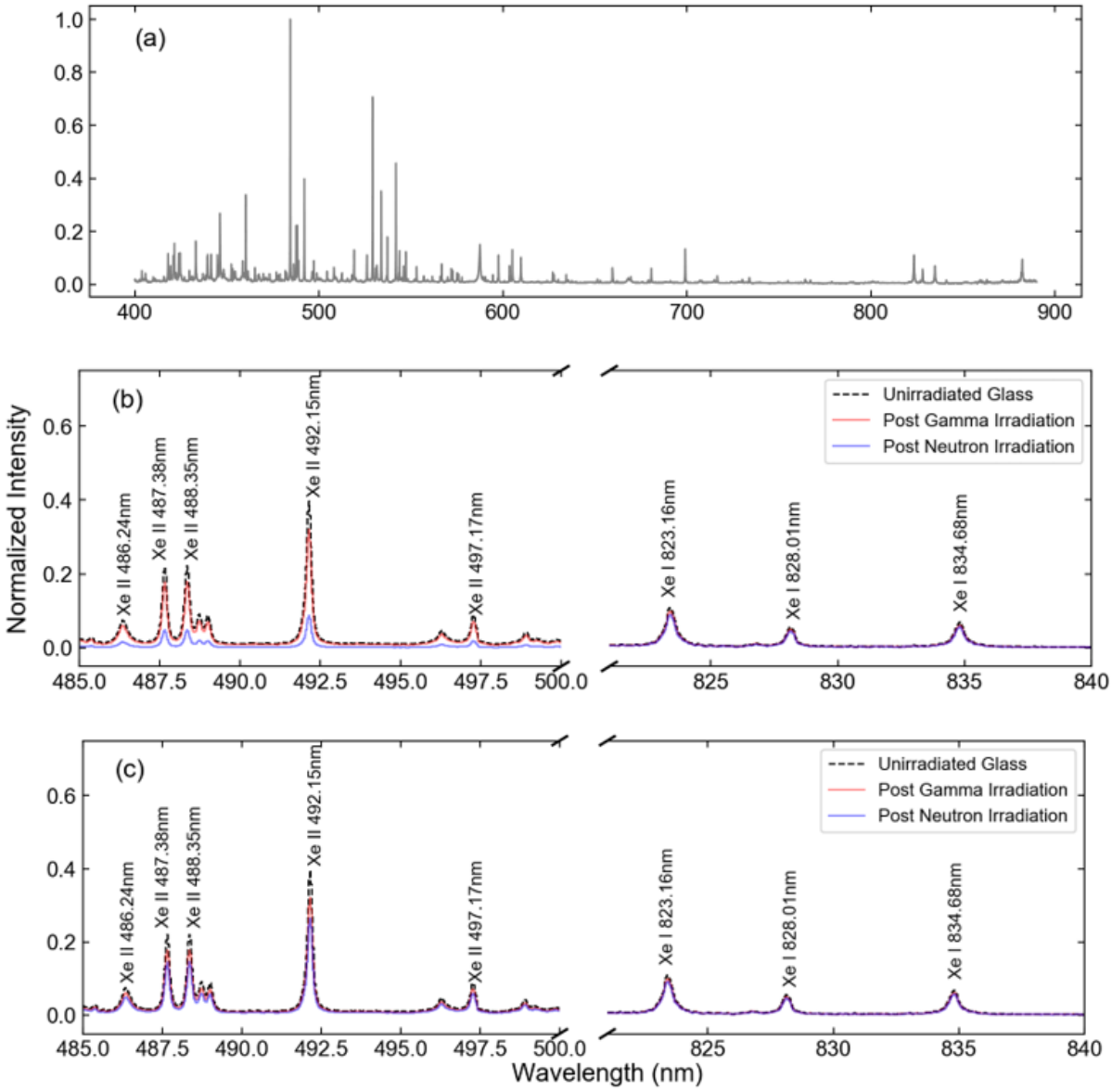

Figure 2: (a) Full measured spectra and the spectra adjusted for the expected linear absorption changes in (b) Infrasil-302 and (c) sapphire windows in the range of 485–500 nm and 825–840 nm

(iStar T334, Andor) was used to record spectra. A gate delay of 1 µs was used to minimize the contribution of continuum radiation while still maintaining an environment conducive to LTE conditions. Additionally, a gate width of 1 µs was selected, allowing for minimal spectral line variation over the collection time [23]. Each spectrum results from the accumulation of 20 laser shots. Wavelength calibrations were performed using an Ar lamp (Pen Light, Oriel).

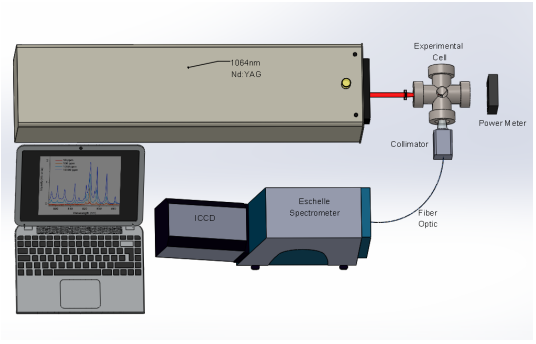

Figure 3: Setup for Xe LIBS measurements

3.2. Linear Absorption Measurements

The optical absorption was measured by irradiating the Infrasil-302 fused-silica glass and sapphire (Heraeus) in the dry tubes of the Co-60 irradiator located at the Nuclear Reactor Laboratory (Ohio State University) and in the water pools of the research reactor at the Radiation Science and Engineering Center (Pennsylvania State University). For the gamma irradiation, the Infrasil-302 glass received a total dose of 10 Mrad, while the sapphire received a total dose of 3.6 Mrad. For the neutron irradiation, samples were exposed to combined neutron and gamma radiation with fluences of 3.4×10^{16} neutrons/cm^2 and 1.7×10^{17} neutrons/cm^2, respectively. Absorption was measured using a broadband light source (DH-2000-BAL, Ocean Insight) and UV-NIR spectrometer (HR-4000 CG-UV-NIR, Ocean Insight). Further details on this measurement can be found in Ref. [12, 13].

4. Results and Discussion

Figure 2 shows the calculated effect on the spectrum if light were to travel through a 1.2-cm window made of the materials investigated after receiving the maximum dosage for each irradiation method. While all cases demonstrate more significant effects at lower wavelengths, the exposure to high neutron fluxes proved to be detrimental in the detection of spectral lines in the important region of 400–500 nm, where the majority of Xe II emission is found. It can be noted, however, that minimal effects are observed in the near-IR spectral region, where the Xe I spectral emission is located; suggesting that it may be beneficial to focus calculations basing on the Xe I lines since the attenuation is nearly constant and over 75% of the line intensity is maintained.

Table 2 shows the changes to the single line detectability as a function of received radiation dose for select Xe transitions. For the gamma irradiations, the transmission of all lines over 400 nm remains above 75% for both tested materials, resulting in negligible changes to the number of laser shots required to meet the 3σ detection criterion. In contrast, the line attenuation resulting from neutron damage leads to up to a 10× increase in the minimum number of laser shots to meet the 3σ detection criterion. Due to the high repetition rate from the available laser systems, the required measurement time in these cases would remain tolerable. For example, for the laser used in this study that operates at 10 Hz, all measurement times would remain shorter than 1 second.

Figure 4 and Table 3 compare how the observed line intensity ratios for the Xe I 828.0-nm emission and Xe II 484.4-nm emission to the He I 587.6-nm change for different window materials and radiation doses. Due to the increased attenuation at shorter wavelengths, the radiation-induced attenuation reduces the line intensity ratio of short wavelength Xe emissions and increases the line ratio for long wavelength Xe emissions compared to the true value.

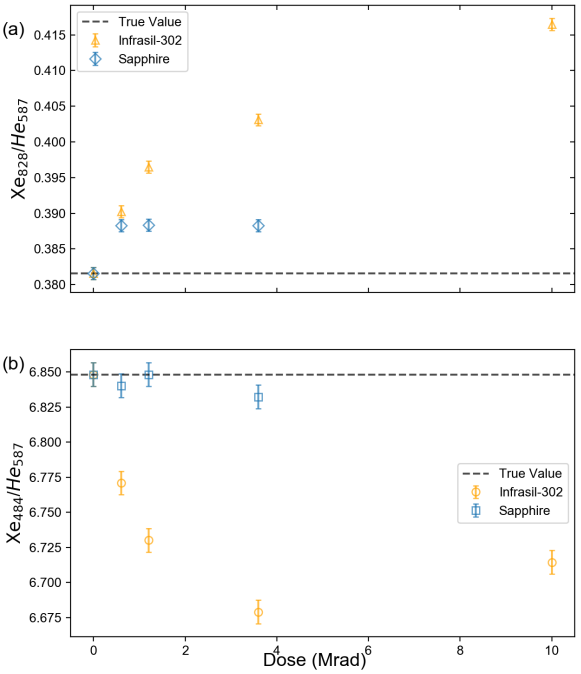

Figure 4: Gamma dose dependence of (a) intensity ratio of 828-nm Xe I line and 587-nm He I line; (b) intensity ratio of 484-nm Xe II line and 587-nm He I line

Boltzmann and Saha-Boltzmann plots are constructed by selecting the Xe I and Xe II lines that are resolvable, could be attributed to a single transition, and when possible had relatively high upper level energies (Table 1) [28]. Figure 5 displays the calculated Boltzmann plots for the Xe I and Xe II lines separately, while Figure 6 displays the Saha-Boltzmann plots for both the original data and the radiation-induced attenuation-corrected data. The LTE assumption is supported for the calculated plasma density of $2.25\pm0.35\times10^{17}$ cm^{-3}, which meets the McWhirter Criterion [16, 29]. This value was calculated by averaging the plasma density calculated individually for the 484.4 nm, 541.9 nm, 603.6 nm, and 605.1 nm lines associated with Xe II using the Stark data published by Konejevic [30, 31] and the Lorentzian component of their respective FWHM

Table 1: Wavelength, transition probability, degeneracy, and upper and lower energy levels of Xe transitions according to NIST [25–27]

Species	**Wavelength**	**Einstein coeff.**	**Lower level**		**Upper level**	
	(nm)	($10^7 s^{-1}$)	Degeneracy	Energy (eV)	Degeneracy	Energy (eV)
Xe I	764.202	2.1	1	9.4472	3	11.0691
	828.012	3.69	3	8.4365	1	9.9335
	834.682	4.2	3	9.5697	5	11.0547
	840.919	0.306	5	8.3153	3	9.7893
Xe II	433.052	14	6	14.0737	8	16.9360
	484.433	11	6	11.5390	8	14.0977
	487.650	6.3	6	13.5841	8	16.1259
	526.044	2.2	2	12.9254	4	15.2816
	526.195	8.5	4	14.0009	4	16.3565
	627.082	1.8	4	14.0009	6	15.9775

Table 2: The minimum number of laser shots a 3σ detection level for the examined materials as a function of the irradiation method and received dose.

Spectral Line	**Irradiation Condition**	**Shots for 3σ**
828.0 nm	Unirradiated	1±1
	Infrasil γ Irradiation	2±2
	Infrasil n Irradiation	4±2
	Sapphire γ Irradiation	1±1
	Sapphire n Irradiation	1±1
484.4 nm	Unirradiated	1±1
	Infrasil γ Irradiation	2±2
	Infrasil n Irradiation	17±5
	Sapphire γ Irradiation	1±1
	Sapphire n Irradiation	5±3

Table 3: Neutron flux dependence of the line intensity ratios

Sample	**Flux (n/cm^2)**	**I_{828}/I_{587}**	**I_{484}/I_{587}**
Infrasil-302	0 (Unirradiated)	0.382±0.0008	6.74±0.008
	3.4×10^{16}	0.497±0.0008	7.24±0.009
	1.7×10^{17}	1.45±0.0009	9.46±0.009
Sapphire	0 (Unirradiated)	0.382±	6.84±0.008
	3.4×10^{16}	0.509±0.0008	6.51±0.007
	1.7×10^{17}	6.93±0.007	4.57±0.009

values. This value was found to be in good agreement with the density as calculated by the Saha-Eggert equation (Eq 2.2) where a density of approximately 9×10^{16} cm^{-3} was calculated. Error bars reflect the 95% confidence interval around the calculated temperature, as determined from the slope produced from linear regression. The changes in calculated temperature and the fit error resulting from attenuation corrections are shown in Table 4. When the Xe I lines alone are used, no significant change in temperature is noted, due to the nearly uniform reduction in line intensities. As a result, the line slope from which the temperature is calculated remains nearly constant. In contrast, significant changes can be observed when only Xe II lines are used, since they are located in more strongly attenuated spectral regions and span a greater spectral range. While the observed differences can be mitigated if the ionic line corrections are applied within the Saha-Boltzmann plot, the irradiation-induced attenuation acts to reduce the goodness of fit for the linear regression, as evidenced by the decrease in the associated R^2 value and increased fitting error.

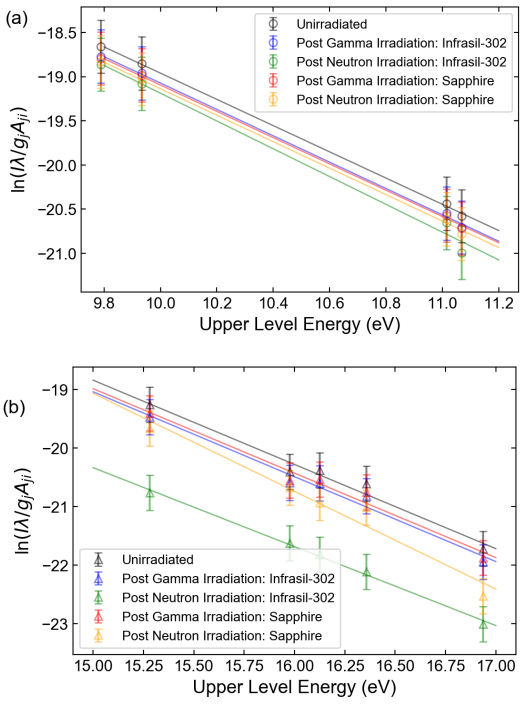

Figure 5: Boltzmann plots using the spectral data both before and after accounting for radiation-induced attenuation for (a) Xe I lines only and (b) Xe II lines only.

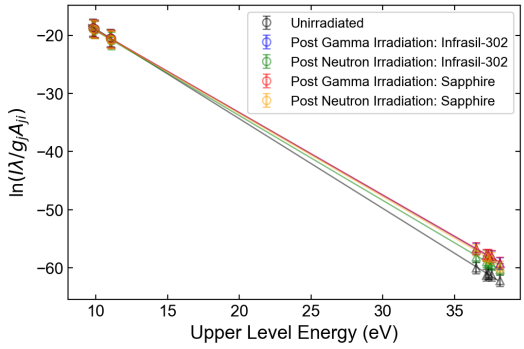

Figure 6: Saha-Boltzmann plot using the spectral data before and after accounting for radiation-induced attenuation. Circles represent points originating from Xe I transitions, while triangles denote points originating from Xe II transitions.

Table 4: Comparison of the calculated temperatures for both the Boltzmann plot and Saha-Boltzmann plot

Method	Irradiation Condition	Temperature (K)	R^2
Xe I Boltzmann	Unirradiated	7810±390	0.9993
	Infrasil γ Irradiation	7770±390	0.9990
	Infrasil n Irradiation	7370±410	0.9909
	Sapphire γ Irradiation	7800±390	0.9992
	Sapphire n Irradiation	7740±400	0.9987
Xe II Boltzmann	Unirradiated	8000±610	0.9779
	Infrasil γ Irradiation	8000±850	0.9755
	Infrasil n Irradiation	8600±890	0.9960
	Sapphire γ Irradiation	8000±840	0.9759
	Sapphire n Irradiation	6900±880	0.9603
Saha-Boltzmann	Unirradiated	7900±350	0.9983
	Infrasil γ Irradiation	8100±460	0.9981
	Infrasil n Irradiation	7660±500	0.9978
	Sapphire γ Irradiation	8000±410	0.9981
	Sapphire n Irradiation	8100±490	0.9981

5. Conclusion

We used the linear absorption data from the gamma and neutron irradiation of fused-silica glass and sapphire windows to investigate the effect on the quantities derived from the analysis of LIBS spectra in which the emitted light travels through one of these materials. For a LIBS measurement of Xe in an ambient He environment, it was found that for spectral lines which experience the most significant attenuation, the required number of laser shots to detect the line with the same statistical certainty increases from 1 to 10 shots, while the detectability of lines that are minimally attenuated remains largely unchanged. However, the repetition rate of commercially available lasers allows for measurement times in the investigated case to remain relatively short, on the order of seconds. This effect may be more pronounced if analysis were based on less prominent spectral lines. The nonuniform attenuation across the spectrum was found to have more noticeable effects on calculations that rely on the comparison of line intensity ratios, effectively overestimating the Xe/He line ratio of shorter-wavelength Xe spectral lines such as the 484.4-nm Xe II line and underestimating the line ratio of longer-wavelength Xe lines such as the 828.0-nm Xe I line. This effect also manifests in the calculation of temperature using Boltzmann plots such that the error on the resultant temperature value increases.

The results of this study suggest that the observed effects may be negligible or mitigated through the introduction of additional calibrations for spectral lines relevant to helium-cooled fast reactors. However, it must be noted that the Xe concentration used is significantly greater than what would be expected within a reactor coolant stream during standard operation. This likely greatly improves the predicted single-line detectability observed. To more accurately predict the effects within a reactor environment, the same analysis could be applied to a spectrum resulting from ppm to ppb concentrations of Xe as well as a spectrum that includes other expected fission fragments to help account for matrix effects [17, 32]. In addition, studies suggest that effects of thermal annealing, which may occur concurrently within the glass, depending on the proximity to the reactor high temperatures of the reactor core, can repair some of the radiation damage observed [12, 13]. Therefore, corrections must also consider the these effects. Other future work may include the analysis of spectra relevant to other nuclear reactor monitoring applications such as examining the radiation-induced attenuation effect on spectral lines that have been proposed for monitoring impurities in molten salt-cooled reactors [1].

Declaration of Competing Interests

The authors declare that they have no known competing financial interests or personal relationships that could have appeared to influence the work reported in this paper.

Acknowledgements

This work was supported by the Department of Energy, Nuclear Science User Facilities (DE-NE0008906); U.S. Department of Defense (HDTRA1-20-2-0002); B. W. M (Army Advanced Civil Schooling Program).

This work was conducted in conjunction with the Versatile Test Reactor project and is based upon work supported by the U.S. Department of Energy under Prime

Contract No. DE-AC07-05ID14517 to the Idaho National Laboratory. Any opinions, findings, and conclusions or recommendations expressed in this publication are preliminary and are those of the author(s) and do not necessarily reflect the views of the U.S. Department of Energy or the Idaho National Laboratory.

This research was performed under appointment to the Nuclear Nonproliferation International Safeguards Fellowship Program sponsored by the Department of Energy, National Nuclear Security Administration's Office of International Nuclear Safeguards (NA-241).

References

[1] A. Williams, S. Phongikaroon, Laser-induced breakdown spectroscopy (libs) measurement of uranium in molten salt, Appl. Spectrosc. 72 (2018) 1029–1039.

[2] M. Burger, L. Garrett, A. Burak, V. Petrov, A. Manera, P. Sabharwall, X. Sun, I. Jovanovic, Trace xenon detection in helium *via* laser-induced breakdown spectroscopy, J. Anal. At. Spectrom. 36 (2021) 824–828.

[3] H. Andrews, K. Myhre, Quantification of lanthanides in a molten salt surrogate off-gas stream using laser-induced breakdown spectroscopy, Appl. Spectrosc. (2022).

[4] H. Andrews, J. MacFarlane, K. Myhre, Monitoring noble gases (xe and kr) and aerosols (cs and rb) in a molten salt reactor surrogate off-gas stream using laser-induced breakdown spectroscopy (libs), Appl. Spectrosc. (2022).

[5] Y. Lee, S. Yoon, N. Kim, D. Kang, H. Kim, W. Yang, M. Burger, I. Jovanovic, S. Choi, In-situ measurement of ce concentration in high-temperature molten salts using acoustic-assisted laser-induced breakdown spectroscopy with gas protective layer, Nucl. Eng. Technol. in-press (2022).

[6] D. Cremers, L. Radziemski, Handbook of Laser-Induced Breakdown Spectroscopy, John Wiley Sons, New Jersey, 2013.

[7] R. Russo, X. Mao, J. Gonzalez, V. Zorba, J. Yoo, Laser ablation in analytical chemistry, Anal. Chem. 85 (2013) 6162–6177.

[8] D. Rusak, B. Castle, B. Smith, J. Winefordner, Fundamentals and applications of laser-induced breakdown spectroscopy, Crit. Rev. Anal. Chem. 27 (1997) 257–290.

[9] W. Primak, E. Edwards, Radiation-induced dilations in vitreous silica, Phys. Rev. 128 (1962) 2580–2588.

[10] W. Primak, J. Luthra, Radiation induced expansion and increase in refractive index of magnesium oxide; evidence for the f center, Phys. Rev. 39 (1966) 5651–5658.

[11] G. Sharma, K. Thind, Manupriya, H. Klare, S. Narang, L. Gerward, V. Dangwal, Effects of gamma-ray irradiation on optical properties of zno-pbo-b_2o_3 glasses, Nucl. Instrum. Methods Phys. Res. B 243 (2006) 345–348.

[12] B. Morgan, M. Van Zile, P. Sabharwall, M. Burger, I. Jovanovic, Gamma-radiation-induced negative nonlinear absorption in quartz glass, Opt. Mater. Express 36 (2022) 1188–1197.

[13] B. Morgan, M. Van Zile, C. Petrie, P. Sabharwall, M. Burger, I. Jovanovic, Optical absorption of fused silica and sapphire exposed to neutron and gamma radiation with simultaneous thermal annealing, J. Nucl. Mater. 507 (2022).

[14] D. Tudor, J. Vaughan, A new tabulation of the voigt profile, Astrophys. J. 137 (1963) 1302–1305.

[15] E. Whiting, An empirical approximation to the voigt profile, J. Quant. Spectrosc. Radiat. Transfer 8 (1968) 1379–1384.

[16] H. Griem, Principles of Plasma Spectroscopy, Cambridge University Press, New York, 1997.

[17] J. El Haddad, L. Canioni, B. Bousquet, Good practices in libs analysis: Review and advices, Spectrochim. Acta B: At. Spectrosc. 101 (2014) 171–182.

[18] M. Essien, L. Radziemsky, J. Sneddon, Detection of cadmium, lead and zinc in aerosols by laser-induced breakdown spectrometry, J. Anal. At. Spectrom. 3 (1988) 985–988.

[19] M. Joseph, N. Xu, V. Majidi, Time-resolved emission characteristics and temperature profiles of laser-induced plasmas in helium, Spectromchim. Acta B: At. Spectrosc. 49 (1994) 89–103.

[20] C. Aragón, F. Peñalba, J. Aguilera, Spatial characterization of laser-induced plasmas: distributions of neutral atom and ion densities, Appl. Phys. A 79 (2004) 1145–1148.

[21] C. D. Yalçin, Ş, G. Smith, G. Faris, Influence of ambient conditions on the laser air spark, Appl. Phys. B 68 (1999) 121–130.

[22] J. Aguilera, C. Aragón, Mult-element saha-boltzmann and boltzmann plots in laser-induced plasmas, Spectrochim. Acta B: At. Spectrosc. 62 (2007) 378–385.

[23] G. Cristoforetti, A. De Giacomo, M. Dell'Aglio, S. Legnaioli, E. Tognoni, V. Palleschi, N. Omenetto, Local thermodynamic equilibrium in laser-induced breakdown spectroscopy: Beyond the mcwhirter criterion, Spectrochim. Acta B: At. Spectrosc. 65 (2010) 86–95.

[24] M. Burger, J. Hermann, Stark broadening measurements in plasmas produced by laser ablation of hydrogen containing compounds, Spectrochim. Acta B: At. Spectrosc. 122 (2016) 118–126.

[25] J. Sabbagh, N. Sadeghi, Experimental transition probabilities of some xe(i) lines, J. Quant. Spectrosc. Radiat. Transfer 17 (1977) 297–301.

[26] R. Shuker, Y. Binur, A. Szöke, Studies of afterglow in noble-gas mixtures: A model for energy transfer in he/xe, Phys. Rev. A 12 (1975).

[27] J. Fuhr, W. Wiese, CRC Handbook of Chemistry and Physics, CRC Press, Boca Raton, Florida, 79th edition, 1998.

[28] L. Sun, H. Yu, Correction of self-absorption in calibration-free laser-induced breakdown spectroscopy by an internal reference method, Talanta 2009 (2009) 288–395.

[29] I. Hutchinson, Principles of Plasma Diagnostics, Cambridge University Press, New York, 2nd edition, 2002.

[30] N. Konjevic, M. Dimitrijevic, W. Wiese, Experimental stark widths and shifts for spectral lines and neutral atoms (a critical review of selected data for the period 1976 to 1982, J. Phys. Chem. Ref. Data 13 (1984) 619–647.

[31] N. Konjevic, A. Lesage, J. Fuhr, W. Wiese, Experimental stark widths and shifts for spectral lines of neutral and ionized atoms (a critical review of selected data for the period 1989 through 2000, J. Phys. Chem. 31 (2002) 819–927.

[32] D. Hahn, N. Omenetto, Laser-induced breakdown spectroscopy (libs), part i: Review of basic diagnostics and plasma-particle interactions: Still-challenging issues within the analytical plasma community, Appl. Spectrosc. 64 (2010) 335A–366A.